Published OnlineFirst April 6, 2010; DOI: 10.1158/1535-7163.MCT-09-0829

Research Article

Molecular Cancer Therapeutics

A Molecularly Targeted Theranostic Probe for Ovarian Cancer

Wenxue Chen[1,6], Rizia Bardhan[3], Marc Bartels[1], Carlos Perez-Torres[2], Robia G. Pautler[1,2], Naomi J. Halas[3,4,5], and Amit Joshi[1]

Abstract

Overexpression of the human epidermal growth factor receptor (HER) family has been implicated in ovarian cancer because of its participation in signaling pathway regulating cellular proliferation, differentiation, motility, and survival. Currently, effective diagnostic and therapeutic schemes are lacking for treating ovarian cancer, and consequently ovarian cancer has a high mortality rate. Although HER2 receptor expression does not usually affect the survival rates of ovarian cancer to the same extent as in breast cancer, it can be used as a docking site for directed nanotherapies in cases with *de novo* or acquired chemotherapy resistance. In this study, we have exploited a novel gold nanoshell–based complex (nanocomplex) for targeting, dual modal imaging, and photothermal therapy of HER2-overexpressing and drug-resistant ovarian cancer OVCAR3 cells *in vitro*. The nanocomplexes are engineered to simultaneously provide contrast as fluorescence optical imaging probe and a magnetic resonance imaging agent. Immunofluorescence staining and magnetic resonance imaging successfully show that nanocomplex–anti-HER2 conjugates specifically bind to OVCAR3 cells as opposed to the control, MDA-MB-231 cells, which have low HER2 expression. In addition, nanocomplexes targeted to OVCAR3 cells, when irradiated with near-IR laser, result in selective destruction of cancer cells through photothermal ablation. We also show that near-IR light therapy and the nanocomplexes by themselves are noncytotoxic *in vitro*. To the best of our knowledge, this is the first successful integration of dual modal bioimaging with photothermal cancer therapy for treatment of ovarian cancer. Based on their efficacy *in vitro*, these nanocomplexes are highly promising for image-guided photothermal therapy of ovarian cancer, as well as other HER2-overexpressing cancers. *Mol Cancer Ther; 9(4); 1028–38. ©2010 AACR.*

Introduction

Epithelial ovarian cancer is the most lethal gynecologic malignancy and is the fourth most frequent cause of cancer-related death of women in Western countries. In 2008, there were 21,650 new cases of ovarian cancer and 15,520 deaths reported in the United States (1). However, the difficulty in detecting ovarian cancer at an early stage, aggressiveness, and the lack of effective therapy contribute to high mortality (2). Advanced ovarian cancers have primarily clinical prognostic factors: patient performance status, tumor volume, stage, dissected residual tumor size, and ascites. However, most prognostic models proposed in the literature do not include biological factors (3). In 2004, in a study on human epidermal growth factor receptor 2 (HER2) overexpression in ovarian cancer, Camilleri-Broët and coworkers (4) used immunohistochemical evaluation on paraffin-embedded tissues to determine the prognostic impact of HER2 protein level. They found on multivariate analysis that HER2 overexpression was an independent predictor of overall and disease-free survival. HER2 is frequently overexpressed in ovarian cancer patients; the overexpression rate has been reported in a wide range from 8% to 66% (4–8). The 66% figure was reported by fluorescence *in situ* hybridization study in 74 cases (8); 53% in 181 cases (7), 22% in 23 cases (6), and 16% in 95 cases (4). Dimova (5) analyzed multiple samples applying the highly reliable method of fluorescence *in situ* hybridization on tissue microarray, containing 1,006 ovarian tumors and reported 8% HER2 amplifications in ovarian malignant epithelial tumors. HER2 overexpression is associated with a poor prognosis due to acquired chemotherapy resistance. The HER2-positive cell line OVCAR3 was chosen because it wasisolated from a malignant effusion and is resistant to clinically relevant doses of cyclophosphamide, Adriamycin, melphalan, and cisplatin (9, 10) and is a good candidate for showing molecularly targeted and image-guided phototherapy.

The design and development of novel nanoagents that synergistically incorporate multiple functionalities,

Authors' Affiliations: [1]Department of Radiology and [2]Molecular Physiology and Biophysics, Baylor College of Medicine; Departments of [3]Chemistry, [4]Electrical and Computer Engineering, and [5]Bioengineering, Rice University, Houston, Texas; and [6]Department of Obstetric and Gynecology, the Fourth Hospital of Hebei Medical University/Hebei Province Tumor Hospital, Shijiazhuang, Hebei Province, China

Note: W. Chen and R. Bardhan contributed equally to this work.

Corresponding Author: Amit Joshi, Baylor College of Medicine, BCM 360, 1 Baylor Plaza, Houston, TX 77030. Phone: 7137989191; Fax: 7137988050. E-mail: amitj@bcm.edu

doi: 10.1158/1535-7163.MCT-09-0829

Published OnlineFirst April 6, 2010; DOI: 10.1158/1535-7163.MCT-09-0829

including targeting, imaging, and therapy, all within the same nanoprobe is emerging rapidly as an impending alternative to traditional therapeutic drugs and imaging agents (11). This promising new paradigm is hence termed as "theranostic," which entails the efficient integration of therapeutic and diagnostic moieties into a single nanoagent. Nanoparticles in the size range of 5 to 250 nm are effective interventional agents for cancer because of their unique size, which allows passive accumulation in tumors, and because of their ability to carry multiple diagnostic and therapeutic payloads. Most clinical trials involving nanoparticles focus on targeted chemotherapy delivery (12) because, despite the emerging molecular medicine–based shift toward cancer-specific cytostatic agents, cytotoxic chemotherapy is still considered more effective against broad patient populations. Although nanocarrier-based chemotherapy can minimize traditional side effects, it is not externally controlled, and in the case of liposomes, which have been approved since the 1990s, the inability to guarantee intracellular drug delivery often results in treatment failure.

Alternative cancer therapeutics based on the photothermal response of gold nanostructures designed to absorb near-IR, tissue-penetrating light has exhibited near 100% efficacy in the remission of tumors and stands as one of the most promising new technologies to emerge from nanoscience research in the past decade. Following the initially shown therapeutic success of gold nanoshells, other gold nanoparticles, such as gold nanorods, hollow gold nanospheres, and gold nanocages, have also been used to show similar, highly promising therapeutic responses (13–17). Gold-based nanostructures show particular promise as theranostic agents based on their straightforward adaptability to integrate targeting, diagnostic, and therapeutic functionalities into a single, hybrid, multifunctional nanoscale complex (18, 19). Silica core gold nanoshells with plasmon resonance in near-IR region effectively absorb near-IR light and generate hyperthermia for externally controlled tumor cell death (14, 18, 20). Similarly superparamagnetic iron oxide particles can be exposed to alternating magnetic fields for tumor hyperthermia (21). At present, nanoshells cannot be directly imaged in deep tissue because only indirect-absorbing/scatter-based contrast has been exploited. Although highly sensitive, noninvasive near-IR imaging is constrained by limited photon penetration in tissue and cases such as cancer metastasis in deep axillary lymph nodes, and organs, such as ovary, lungs, liver, skeleton, and brain, will be outside its purview for the foreseeable future. Magnetic resonance imaging does not have tissue depth constraints, but superparamagnetic iron oxide particles require heavy tumor loading for imaging and therapy (21), and if surgery is needed, they do not provide any intraoperative guidance for tumor margin determination. The complementary capabilities of near IR and magnetic resonance imaging provide the motivation for combining near-IR light and magnetic field–based imaging and therapy in one nanoparticle. Gold nanostructures with integrated near-IR emitters for fluorescence enhancement of optical tomography and with iron oxide nanoparticles for magnetic resonance imaging enhancement can serve as simultaneous theranostic reporter-actuators. With antibody or peptide conjugation, this theranostic hybrid nanoparticle can be delivered to specific cells or tissues for therapy, with reporter functionalities providing tracking capabilities before, during, and after treatment. Recently, some theranostic nanoprobes have been synthesized with complex geometries (22–26); however, their capability has been mostly limited to a single imaging modality such as either magnetic resonance imaging or optical imaging. Recently, we designed and used a multifunctional gold nanoshell–based theranostic complex (nanocomplex) to actively target, image through magnetic resonance imaging and fluorescence optical imaging, and induce photothermal tumor ablation in breast cancer cells with near-IR illumination (27). In this study, we show the efficacy of these nanocomplexes for simultaneous diagnosis and therapy of ovarian cancer cells *in vitro* and further show the nontoxicity of near-IR therapy and the nanocomplexes.

The nanocomplex consist of a gold (Au) nanoshell encapsulated in a silica (SiO_2) shell, which is doped with superparamagnetic iron oxide and a near-IR emitting fluorophore, indocyanine green. Au nanoshells are optically tunable nanoparticles that consist of a SiO_2 core surrounded by a thin Au shell (28). Based on the relative dimensions of the shell thickness and core radius, nanoshells can be designed to scatter and/or absorb light over a broad spectral range, including the near IR. The near-IR wavelength region provides maximal penetration of light through soft tissue, including hypoxic regions in tumors, and irradiation of tumors with near-IR laser light can lead to thermal ablation (29). The nanoshells enhance the fluorescence of indocyanine green molecules incorporated into the outer layer of the nanocomplex. Indocyanine green is a Food and Drug Administration–approved fluorescent emitter with a quantum yield of ~1.3% in aqueous media. When incorporated into the oxide layer just outside the gold shell layer, the nanoshell enhances the fluorescence quantum yield by nominally 4,500%, resulting in a very bright near-IR fluorescent probe (30). The nanoscale superparamagnetic iron oxide layer concurrently provides a high magnetic resonance contrast, thus enabling multimodal imaging with the same agent. Accumulation of nanoshells in tumor cells can be achieved through passive extravasation based on the enhanced permeability and retention of small particles associated with the leaky tumor vasculature (31). However, when targeted using antibodies against oncoproteins over expressed on cell surfaces, a higher concentration of nanoshells can be selectively bound to cell surfaces and enable extended periods of diagnostic imaging, as well as therapy.

The photothermal properties of nanoshells are attributed to their ability to absorb near-IR light at their plasmon resonant wavelength because of their large absorption cross-section, efficiently converting the light energy to

Published OnlineFirst April 6, 2010; DOI: 10.1158/1535-7163.MCT-09-0829

heat. The heat generated by the nanoshells raises the local temperature in their direct vicinity, resulting in the thermal ablation of cancer cells (13, 32). In particular, targeted nanoshells will accumulate at the specific tumor site, enabling photothermal therapy of cancer cells only and greatly minimizing damage to adjacent healthy cells. In this study, we have shown that near-IR laser irradiation at low power densities, as well as nanoshells by themselves, are nontoxic and do not induce cytotoxicity. These molecularly targeted nanocomplexes are highly promising and clinically relevant for providing molecule-specific diagnostic information that will enable the detection and treatment of cancer long before phenotypic changes occur. In practice, this will provide an efficient tool for the detection of tumors at an early stage and provide a benign therapeutic strategy for cancer treatment.

Materials and Methods

Nanocomplex fabrication

Au nanoshells [r_1, r_2] = [60, 74] nm were fabricated by seed-mediated electroless plating of Au onto SiO_2 colloidal nanospheres as previously reported (28). Briefly, SiO_2 nanospheres of 60 ± 2 nm radii were synthesized through the Stöber method (33) and then functionalized with (3-aminopropyl) triethoxysilane (Sigma). The aminated silica nanospheres were decorated with small Au colloid (2-3 nm) fabricated by the method reported by Duff et al. (34). A continuous Au shell was grown around the SiO_2 nanospheres by reducing Au from a 1% solution of $HAuCl_4$ in the presence of gaseous CO. Water-soluble superparamagnetic iron oxide (Fe_3O_4) nanoparticles of 10 ± 3 nm diameter were fabricated by following a procedure previously reported (35) and functionalized with (3-aminopropyl) triethoxysilane. The Au nanoshells were then coated with the amine terminated Fe_3O_4 overnight and centrifuged to remove excess Fe_3O_4. The nanoshells coated with the Fe_3O_4 nanoparticles were then encapsulated with silica with the fluorophore indocyanine green doped within the silica layer. Briefly, nanoshells coated with the Fe_3O_4 nanoparticles were mixed with fresh ethanol and 28% NH_4OH (Fisher) and 1 mL ethanolic solution of indocyanine green. Immediately, fresh TEOS was added to the solution mixture, and the vessel was sealed and vigorously stirred for 45 minutes. The nanocomplexes were stored in the refrigerator at 4°C overnight, protected from light. After 24 h, the particles were centrifuged and redispersed in ethanol. The absorbance of the supernatant was monitored to account for unbound indocyanine green in the supernatant. The concentration of the supernatant was then subtracted from the initial concentration of indocyanine green, which was added to calculate the amount of indocyanine green doped within the silica layer. The final nanocomplex concentration after resuspension in ethanol was at ~10^9 particles/mL, and the indocyanine green concentration was ~500 ± 50 nmol/L.

Anti-HER2 conjugation to nanocomplexes

Anti-HER2 (c-erbB-2)/HER-2/neu epitope–specific rabbit antibody 200 μg/mL (Thermo Scientific) was biotinylated with a 1 mmol/L solution of Sulfo-NHS-Biotin (Pierce) at 4°C for 3 hours. After conjugation, the anti-HER2-biotin reagent was dialyzed in PBS (pH 7.2) to remove excess biotin. The nanocomplexes were attached to streptavidin by initially functionalizing with (3-mercaptopropyl) triethoxysilane (Sigma) to generate thiol terminated nanoparticles. These thiol terminated nanoparticles were redispersed in phosphate buffer, mixed with streptavidin maleimide (Sigma) solution, and mildly stirred for 4 hours at 4°C. The streptavidin conjugated nanocomplexes were centrifuged and resuspended in 5 mL phosphate buffer and incubated with biotinylated anti-HER2 at 4°C overnight. The nanocomplexes were centrifuged at 280 g for 5 minutes to remove unbound antibody and finally redispersed in salt-free phosphate buffer (pH 7.2). The number of antibodies per nanocomplex was quantified using enzyme-linked immunosorbent assay (ELISA). The anti-HER2 conjugated nanocomplexes were incubated with horseradish peroxidase–labeled anti-rabbit IgG (Sigma; A0545) for 1 hour after nonspecific reaction sites were blocked with 3% solution of bovine serum albumin (Sigma). The horseradish peroxidase bound nanocomplexes were developed with 3,3′,5,5′-tetramethylbenzidine (Sigma) and compared with a horseradish peroxidase anti-rabbit IgG standard curve ranging from 0.02 to 0.0003125 μg/mL. Results were analyzed using a spectrophotometer (data not shown).

Extinction spectra were obtained using a Cary 5000 UV/visible/near-IR spectrophotometer. The inductively coupled plasma-optical emission spectrometer (ICP-OES) analysis was done using a Perkin Elmer inductively coupled plasma optical emission spectrometer the spectral range of 165 to 800 nm.

In vitro fluorescence optical imaging

OVCAR3 ovarian adenocarcinoma human (*Homo sapiens*) cells and the control cell line MDA-MB-231 breast adenocarcinoma human (*Homo sapiens*) cells were grown in 1× DMEM/F-12 50/50 (Dulbecco's Modified Eagle's Medium/Ham's F-12 50/50 mix with L-glutamine), 1% antibiotics and 10% fetal bovine serum. Cells were incubated at 37°C in a 5% CO_2 environment and were detached from culture with trypsin (0.05%) and EDTA (0.02%) and resuspended in media for passage to wells. Cells (3×10^5) of OVCAR3 and MDA-MB-231 were plated in each well of four well plates, respectively, and allowed to incubate. Subsequently, cells were washed with 1× PBS twice and fixed with 3.7% paraformaldehyde in PBS. Cells were then quenched with lysine-periodate and permeabilized with 0.2% triton, following which they were washed twice with PBS. Normal goat serum (10%) solution was added to each well plate and incubated for 15 minutes, following which excess normal goat serum was removed and the cells were incubated with nanocomplex–anti-HER2 conjugates and unconjugated nanocomplexes at particle concentration

Published OnlineFirst April 6, 2010; DOI: 10.1158/1535-7163.MCT-09-0829

Table 1. Optical filter parameters used for fluorescence microscopy

Dye	Excitation (nm)	Emission (nm)
DAPI	360	470
Alexa Fluor 488	480	530
ICG	720	820
Calcein	480	530
PI	520	620

Abbreviations: ICG, indocyanine green; PI, propidium iodide.

2×10^9 particles/mL for 2 hours at 4°C. After 2 hours, the cells were washed with PBS to remove unbound nanocomplexes, following which the secondary antibody, goat anti-rabbit IgG–Alexa Fluor 488 (Invitrogen) was added to the wells and incubated for 1 hour at 4°C. The cells were again washed with PBS while protected from light for excess secondary antibody removal. The cell plates were then mounted on slides with mounting media containing 4',6-diamidino-2-phenylindole (DAPI; Invitrogen) and prepared for fluorescence imaging.

Fluorescence emission spectra were obtained using Jobin Yvon Fluorolog 3, and the samples were excited at 780 nm. To acquire the fluorescence images, we used a Leica fluorescence microscope (DM6000 B; Leica Microsystems GmbH) with a 100 W xenon lamp and specific filters. The images were obtained using cutoff filters with appropriate excitation and emission wavelengths as listed in Table 1.

In vitro magnetic resonance imaging

Cells (1×10^6) of OVCAR3 and MDA-MB-231 were plated in each well of 60 × 15 mm Style cell culture dishes, respectively, and allowed to incubate. A similar procedure was followed as described in the previous section. After 2 hours of incubation with the nanocomplexes, the cells were washed with PBS, followed by scraping the cells from the bottom of the Petri dish, dispersed in 500 μL PBS, and centrifuged at 1,100 rpm for 5 minutes. The supernatant was then removed leaving ~100 μL cells containing nanocomplex–anti-HER2 conjugates and unconjugated nanocomplexes in the Eppendorf tubes, respectively. Five hundred microliters of 0.5% agarose gel was added to each tube, and the samples were left at 4°C for 10 minutes to allow the agarose to solidify. The tubes containing the solidified agarose gel with OVCAR3 and MDA-MB-231 cells, with the nanocomplex suspended within the gel, were directly used for magnetic resonance imaging.

Magnetic resonance imaging experiments were done on a Bruker Avance Biospec, 9.4 T spectrometer, 21-cm bore horizontal imaging system (Bruker Biospin) with a 35-mm volume resonator. *In vitro* imaging of cells suspended in agarose was done using a three-dimensional rapid acquisition with relaxation enhancement sequence with a repetition time/echo time (TR/TE) equal to 2,000/20 ms with a rapid acquisition with relaxation enhancement factor of 8, leading to an effective TE of 60 ms. Field of view (FOV) was 25.6 × 25.6 × 12.8 mm with an acquisition matrix of 128 × 128 × 64, yielding an isotropic 200 μm resolution.

Maximum intensity projections were created from the three-dimensional magnetic resonance imaging data using a threshold segmentation approach in MATLAB (2008a; The Mathworks). The threshold was set at the average minus twice the SD of the sample. Pixels under this value were considered to be hypointense and are labeled as black in the image. The surrounding normotense agarose is labeled as a transparent light blue. Each hypointense pixel contains a cluster of labeled cells because the scan resolution is not enough to identify individual cells.

In vitro photothermal therapy and cytotoxicity

OVCAR3 and MDA-MB-231 cells were grown in six well plates and incubated with either nanocomplex–anti-HER2 conjugates or unconjugated nanocomplexes, which were already suspended in media appropriate for the cell line at a concentration of 2×10^9 particles/mL. Cells were incubated with nanocomplexes for 2 hours and then washed with PBS three times after changing culture medium directly used for photothermal therapy. Cells were not fixed with 3.7% paraformaldehyde in PBS or quenched with lysine-periodate in these experiments to ensure maximum cell viability. Laser ablation was done using a near-IR laser at 808 nm (L808P200; Thorlabs, Inc.) for 10 minutes at a power density of 5.81 W/cm^2 and a spot size of ~0.8-mm diameter. After irradiation, cells were rinsed gently with PBS and incubated with media for 4 hours. Cell viability was assessed using calcein to stain live cells and propidium iodide to stain dead cells. A dye solution mixture containing 3 μmol/L propidium iodide and 2 μmol/L calcein was prepared, and 150 μL was added to each well with nanocomplexes, which were photothermally ablated. For cytotoxicity studies, cells were incubated with nanocomplexes–anti-HER2 conjugates, unconjugated nanocomplexes, and no nanocomplexes. These cells were not illuminated with the near-IR laser. After incubating the cells with calcein/propidiumiodide mixture for 30 minutes at 37°C, a cover slip was mounted and imaged. In this stain, calcein acetoxymethyl ester (calcein AM) enters the cells and is cleaved by esterases in the live cells to yield cytoplasmic green fluorescence. Dead cells are determined by plasma membrane integrity. This can be assessed in two ways: the ability of a cell to prevent a fluorescent dye from entering it and the ability of a cell to retain a fluorescent dye within it. When a cell dies, its plasma membrane becomes permeable, enabling fluorescent dyes to enter the cell. This allows propidium iodide to enter and bind to nucleic acids, generating a red fluorescence. Propidium iodide is membrane impermeant and generally excluded from viable cells.

Published OnlineFirst April 6, 2010; DOI: 10.1158/1535-7163.MCT-09-0829

Results

A schematic illustration of the nanocomplexes conjugated with antibody is depicted in Fig. 1A. Nanoshells were surrounded with thin (nominally 5-10 nm) epilayers of SiO_2 doped with the fluorophore, indocyanine green, and superparamagnetic iron oxide nanoparticles. This was followed by streptavidin binding and biotinylated anti-HER2 conjugation of the nanocomplex. Normalized extinction spectra of the near-IR resonant nanoshells, nanoshells after coating with Fe_3O_4 and after encapsulating in a silica epilayer, are shown in Fig. 1B. Fluorescence spectra of indocyanine green doped in the silica layer of the nanocomplexes at 833 nm are shown in Fig. 1C. These nanocomplex spectral characteristics provide a better understanding of their functions as imaging probes, as well as a therapeutic agent.

The efficacy of the targeted nanocomplexes–anti-HER2 conjugates to provide image contrast for tumor cells *in vitro* was established by fluorescence optical imaging. Fluorescence images of OVCAR3 cells and MDA-MB-231 cells incubated with nanocomplex–anti-HER2 conjugates and unconjugated nanocomplexes were obtained. MDA-MB-231 breast adenocarcinoma human cells were chosen as a control because of the low levels of HER2 expression present in this cell line (36, 37). Low levels of HER2 expression were used to assign the cell lines into previously clinically defined subtypes, which can be used to guide clinical trial design (38–42). The fluorescence optical images of HER2-positive OVCAR3 cells with nanocomplex–anti-HER2 conjugates are shown in Fig. 2, in which the first column depicts nuclei stained with DAPI (blue), the second column illustrates cytoplasm stained with Alexa Fluor 488–conjugated secondary antibody goat anti-rabbit IgG (green), the third column represents near-IR fluorescence from indocyanine green doped in silica layer of nanocomplexes (red), and the merged image in the last column show the nanocomplexes binding to the cell membrane. After a 2-hour incubation with OVCAR3 cells, the nanocomplex-anti-HER2 conjugates showed specific binding to the cells. The fluorescence images of OVCAR3 cells incubated with the control unconjugated nanocomplexes (without anti-bodies) indicate that the nanocomplexes did not bind to the cells. Because of an absence of the primary antibody (anti-HER2), the secondary antibody did not bind, and no signal was observed from the Alexa Fluor 488 as well. Fluorescence images of low HER2 expressing MDA-MB-231 cells with nanocomplex–anti-HER2 conjugates show less binding in comparison to OVCAR3 cells. Minimal nonspecific binding to the extracellular matrix was observed for the MDA-MB-231 cells, resulting in a very weak near-IR signal from the

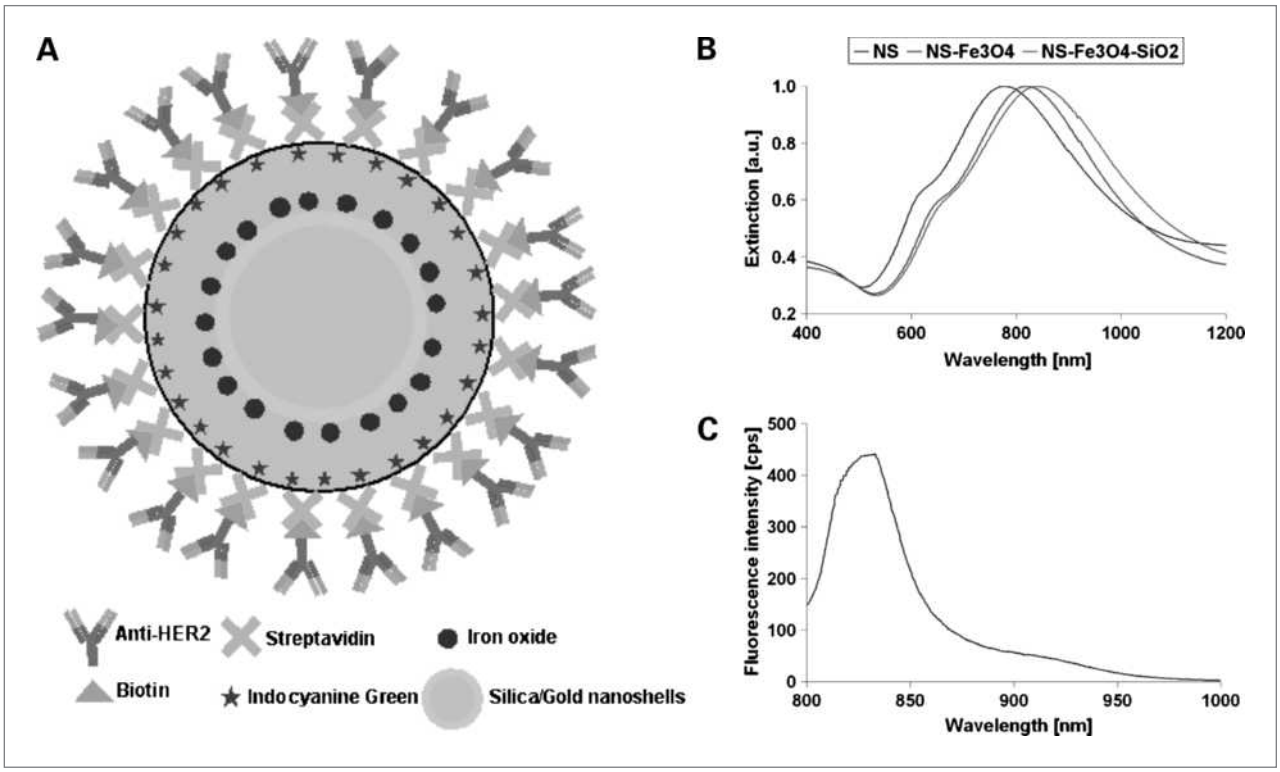

Figure 1. A, schematic representation of anti-HER2–conjugated nanoshell contrast agents. B, extinction spectra of nanoshells (blue) resonant in the near IR at 777 nm, nanoshells after coating with Fe_3O_4 (red) resonant at 821 nm, and after encapsulating in a silica SiO_2 epilayer (green) resonant at 842 nm. NS, nanoshell. C, fluorescence spectrum of indocyanine green doped in the silica layer of the nanoshells at 833 nm.

Published OnlineFirst April 6, 2010; DOI: 10.1158/1535-7163.MCT-09-0829

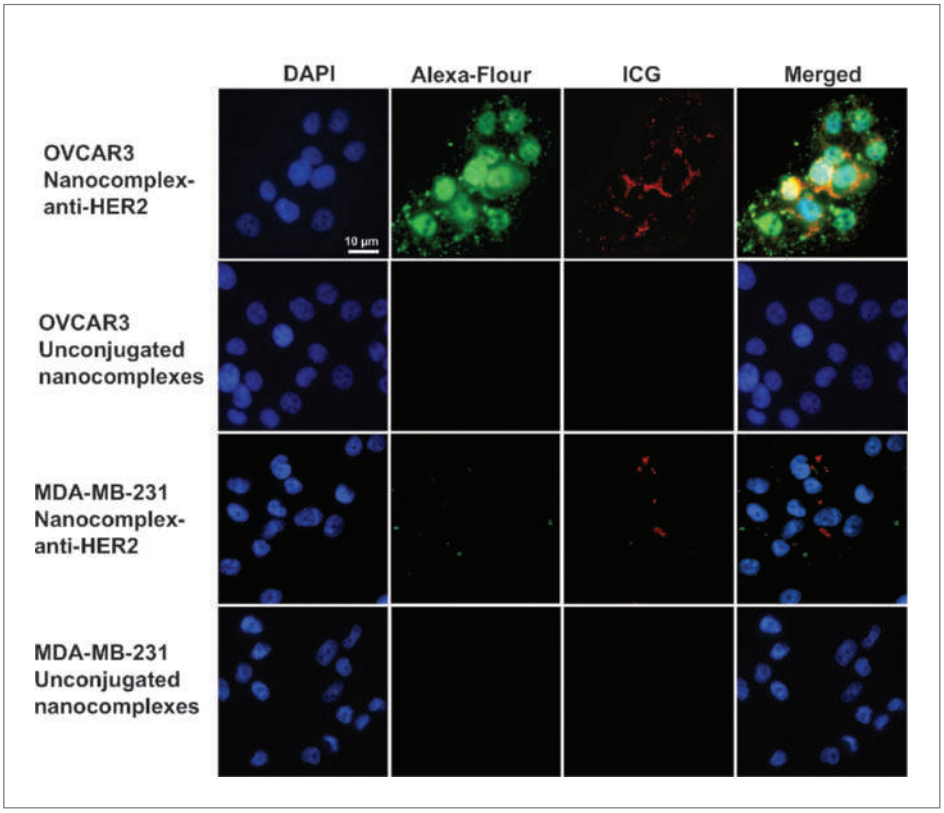

Figure 2. Fluorescence optical images of HER2-positive OVCAR3 cells with nanocomplex–anti-HER2 conjugates (top) showing nuclei stained with DAPI (blue) cytoplasm stained with secondary antibody–Alexa Fluor 488 (green), near-IR fluorescence from indocyanine green doped in silica layer of nanocomplexes (red), and merged image showing the nanocomplex–anti-HER2 conjugates binding outside the cell membrane. Fluorescence images of OVCAR3 cells with the control unconjugated nanocomplexes are in the second row. Fluorescence images of low HER2 expressing MDA-MB-231 cells with nanocomplex–anti-HER2 conjugates and the control are in the third and fourth rows. Some nonspecific binding to the extracellular matrix was observed for MDA-MB-231 cells incubated with the nanocomplex–anti-HER2 conjugates. ICG, indocyanine green. Original magnification, ×400. Scale bar, 10 μm for all panels.

indocyanine green. Similarly, without the primary antibody, the secondary antibody did not bind as well, leading to low fluorescence from Alexa Fluor. The unconjugated nanocomplex incubated with MDA-MB-231 cells also did not bind to the cell membrane. This sequence of experiments shows that the nanocomplex–anti-HER2 conjugates significantly target HER2-overexpressing OVCAR3 cells in comparison to MDA-MB-231 cells, which express low levels of HER2.

The nanocomplex–anti-HER2 conjugates and unconjugated nanocomplexes were incubated with OVCAR3 cells and MDA-MB-231 cells at a concentration of 2×10^9 particles/mL, containing 0.215 mmol/L Fe nanoparticles (determined by ICP-OES). The schematic representation of sample preparation for *in vitro* magnetic resonance imaging studies is shown in Fig. 3A, i. Briefly, cells were incubated with nanocomplexes suspended in media for 2 hours and subsequently centrifuged and redispersed in 0.5% agarose. Optical images of OVCAR3 cells bound to nanocomplex–anti-HER2 conjugates suspended in agarose and OVCAR3 cells with unconjugated nanocomplexes suspended in agarose are shown in Fig. 3A, ii and iii. Magnetic resonance two-dimensional images of OVCAR3 cells suspended in agarose with nanocomplex–anti-HER2 conjugates are shown in Fig. 3B. The cells labeled with nanocomplexes appear as hypointense signals (dark spots) with higher contrast, suggesting that the nanocomplex–anti-HER2 conjugates were bound to the OVCAR3 cells. OVCAR3 cells incubated with unconjugated nanocomplexes showed a few hypointense signals, indicating minimal nonspecific binding. Magnetic resonance images of MDA-MB-231 cells suspended in agarose with nanocomplex–anti-HER2 conjugates clearly show less binding in comparison to OVCAR3 cells. In addition, MDA-MB-231 cells incubated with the control also showed nominal nonspecific binding.

The maximum intensity projections of 128 × 128 × 64 pixel threshold T2 maps, in which each pixel represents the cubic volume of 156 × 156 × 156 μm, are shown in Fig. 3C. The maximum intensity projections were created from the three-dimensional magnetic resonance imaging data using a threshold segmentation approach as described in the *In vitro* Magnetic Resonance Imaging section. The hypointense pixels (brown spots) represent the nanocomplex-labeled cells, and the surrounding normointense pixels (blue) represent the agarose medium. These three-dimensional images correspond to the two-dimensional magnetic resonance images shown directly above. Each hypointense pixel represented here contains a cluster of labeled cells because the scan resolution is insufficient to identify individual cells. The number of hypointense pixels was quantified to determine the specificity and selectivity of the nanocomplex–anti-HER2 conjugates in targeting HER2 expressing cells. The MDA-MB-231 and OVCAR3 cells that had been incubated with the unconjugated nanocomplexes showed

Published OnlineFirst April 6, 2010; DOI: 10.1158/1535-7163.MCT-09-0829

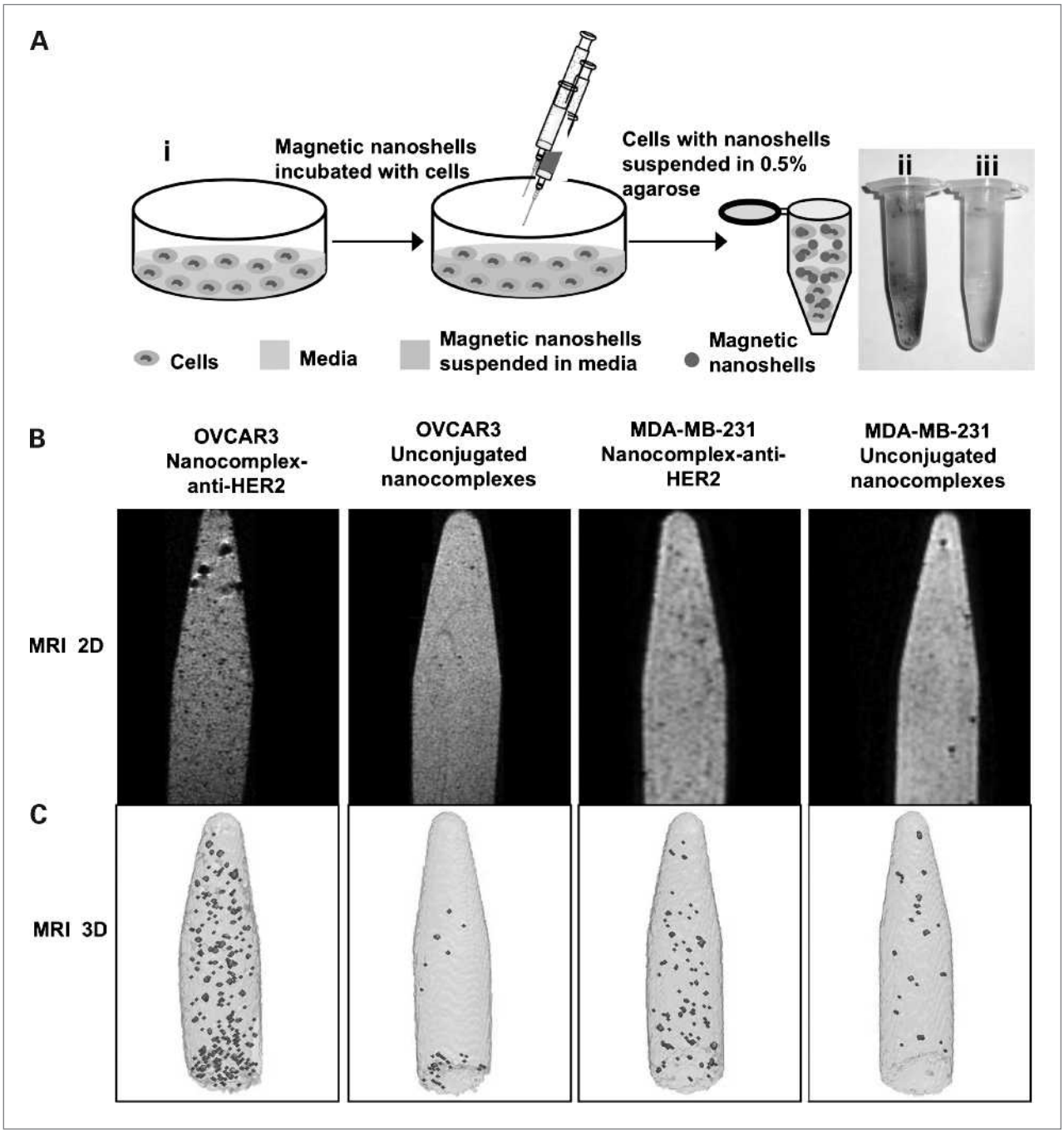

Figure 3. A, i, schematic representation of sample preparation for *in vitro* magnetic resonance imaging studies. Magnetic nanocomplexes are incubated with cells, washed after 2 h, centrifuged, and suspended in 0.5% agarose. Optical image of cells with nanocomplex–anti-HER2 conjugates suspended in agarose (ii) and cells with control unconjugated nanocomplexes suspended in agarose (iii). B, two-dimensional magnetic resonance image of HER2-positive OVCAR3 cells and low HER2 expression MDA-MB-231 suspended in 0.5% agarose with nanocomplex–anti-HER2 conjugates with ~0.215 mmol/L Fe_3O_4 and control unconjugated nanocomplexes. MRI, magnetic resonance imaging. C, maximum intensity projection of 128 × 128 × 64 pixel threshold T2 maps of the images corresponding to the two-dimensional magnetic resonance images. The hypointense signals observed in the two- and three-dimensional images are the cells labeled with the magnetic nanocomplexes.

approximately equal counts of hypointense pixels because of nonspecific binding. The MDA-MB-231 cells incubated with nanocomplex–anti-HER2 had 2.3 times the number of hypointense pixels relative to the cell samples incubated with unconjugated nanocomplexes. In comparison, OVCAR3 cells incubated with nanocomplex–anti-HER2 conjugates had 9.0 times the number of hypointense pixels relative to OVCAR3 cells incubated

Published OnlineFirst April 6, 2010; DOI: 10.1158/1535-7163.MCT-09-0829

with the unconjugated nanocomplexes. OVCAR3 cells incubated with nanocomplex–anti-HER2 conjugates also had 3.1 times the number of hypointense pixels as the MDA-MB-231 cells incubated with the nanocomplex–anti-HER2 conjugates.

The photothermal ablation of OVCAR3 cells incubated with nanocomplex–anti-HER2 conjugates, allowing targeted destruction, is shown in Fig. 4. OVCAR3 and MDA-MB-231 cells incubated with the nanocomplexes–anti-HER2 conjugates and unconjugated nanocomplexes were illuminated with near-IR laser light at 808 nm for 10 minutes at a power density of 5.81 W/cm^2 and a spot size of ~0.8-mm diameter. Following photothermal therapy, cells were stained with the calcein/propidium iodide mixture. Live cells appeared green because of the calcein stain, and dead cells appeared red because of the propidium iodide stain. The nanocomplex–anti-HER2 conjugates, which were bound to the OVCAR3 cell membrane, produced hyperthermia upon laser irradiation, resulting in cell death (Fig. 4A). The increased propidium iodide uptake by the dead cells within the laser spot is clearly observable. MDA-MB-231 cells incubated with nanocomplex–anti-HER2 conjugates were also exposed to the same near-IR laser treatment and showed minimal cell death (Fig. 4C). A small amount of the unconjugated nanocomplex was nonspecifically bound to the OVCAR3 cells and the MDA-MB-231 cells and resulted in some cell death after laser treatment (Fig. 4B, D). Irradiation of OVCAR3 cells treated with nanocomplex–anti-HER2 conjugates with near-IR laser radiation resulted in selective destruction of these cells. In contrast, MDA-MB-231 cells treated with nanocomplex–anti-HER2 conjugates with near IR showed no observable effects on cell viability.

Nanocomplexes by themselves, without photothermal ablation, were observed to be innocuous to cells, and nominal cell cytotoxicity was observed. OVCAR3 cells and MDA-MB-231 cells were incubated with nanocomplex–anti-HER2 conjugates and the unconjugated nanocomplexes for 2 hours, followed by staining with calcein/propidium iodide dye mixture. Cytotoxicity studies on OVCAR3 cells incubated with nanocomplex–anti-HER2 conjugates, unconjugated nanocomplexes, and control (no nanocomplexes) are shown in Fig. 5 (top). Similarly, cytotoxicity studies on MDA-MB-231 cells incubated with nanocomplex–anti-HER2 conjugates, unconjugated nanocomplexes, and control are shown in Fig. 5 (bottom). The

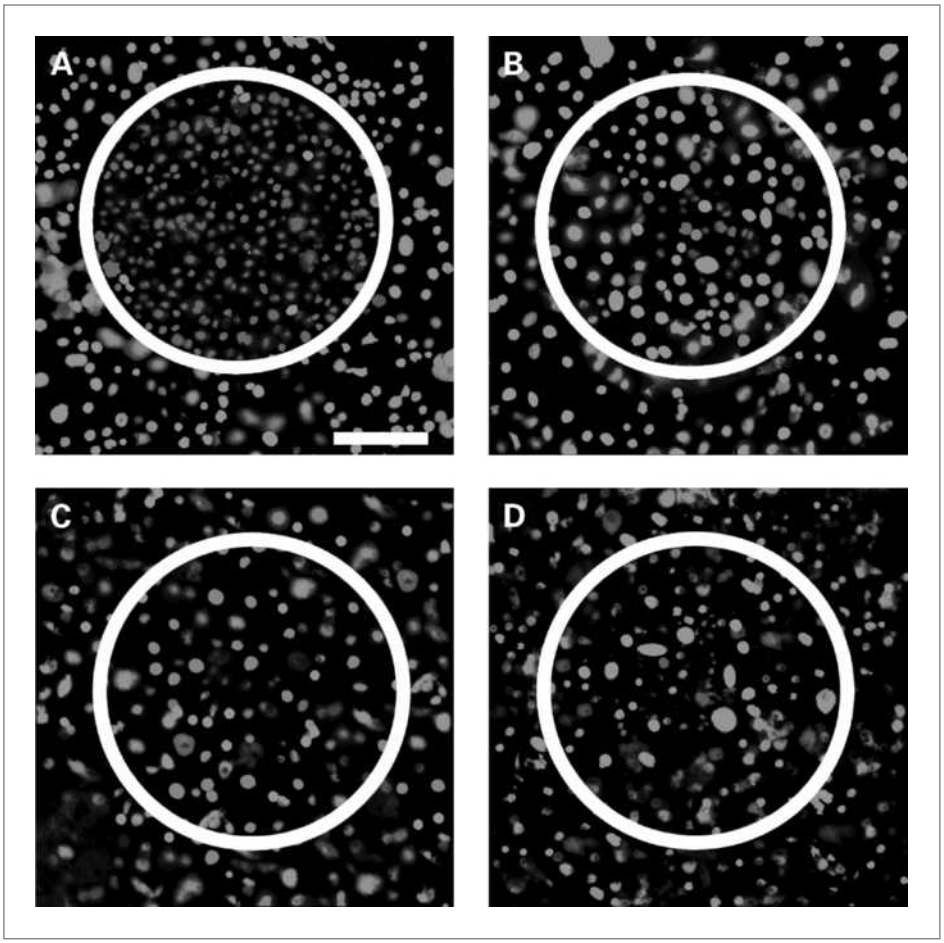

Figure 4. Photothermal ablation and live/dead stain of OVCAR3 cells incubated with nanocomplex–anti-HER2 conjugates (A) and control unconjugated nanocomplexes (B) and treated with near-IR laser at 808 nm for 10 min at a power density of 5.81 W/cm^2 and spot size of ~0.8-mm diameter. Live cells are stained green with calcein and dead cells are stained red with propidium iodide. Similar staining procedure for MDA-MB-231 cells incubated with nanocomplex–anti-HER2 conjugates (C) and control (D) and treated with near-IR laser as well. Original magnification, ×100. Scale bar, 250 μm for all panels.

Published OnlineFirst April 6, 2010; DOI: 10.1158/1535-7163.MCT-09-0829

results for both cell lines are comparable, and minimal differences in cell viability and cell death were observed.

Discussion

Currently, most ovarian cancer diagnoses are for rather advanced stages of the disease because of the lack of availability of early detection and treatment strategies. The standard protocols for the treatment of ovarian cancer have included conventional surgical approaches, followed by chemotherapy or radiation therapy. These standard care treatments often require invasive surgical procedures or other therapies associated with significant side effect profiles, high cost, and poor clinical outcome. Because HER2 receptor amplification occurs in ovarian cancers and is associated with poor clinical outcome, including short survival time and short time to relapse (4–8, 43, 44), it can be targeted with alternative nanoparticle based therapies. Furthermore, HER2-positive cell line OVCAR3 *in vitro* has also been found to be resistant to clinically relevant drugs, including Adriamycin, melphalan, and cisplatin, with survival rates of 43%, 45%, and 77%, respectively, relative to untreated controls (9). The drug resistance of ovary cancer cells can be effectively addressed by image-guided photo/magnetothermal therapies.

The nanocomplexes used here provide a unique platform with targeting, diagnostic, and therapeutic capabilities all within the same agent. There are several advantages offered by these nanoscale agents. First, the nanocomplexes effectively assimilate two imaging modalities, magnetic resonance imaging and fluorescence imaging, which are noninvasive, safe, clinically relevant, and complementary techniques. Although magnetic resonance imaging has the advantage of three-dimensional resolution and visualization of overall anatomic background, it lacks sensitivity. Optical imaging methods such as fluorescence provide high target sensitivity, although they lack three-dimensional resolution. Hence, combining these two imaging modalities synergistically integrates the advantages of the two techniques and overcomes the disadvantages simultaneously. Second, antibody targeting allows nanocomplex–anti-HER2 conjugates to specifically bind to HER2-overexpressing cell surface receptors. Here, immunofluorescence staining and magnetic resonance imaging successfully show that nanocomplex–anti-HER2 conjugates bind to HER2-overexpressing OVCAR3 cells in contrast to MDA-MB-231 cells, which have low HER2 expression. Some nonspecific binding was observed for the unconjugated nanocomplexes. This could be attributed to the overall negative charge on the outer surface of the silica layer of the nanocomplex, as a consequence of the fabrication procedure, which interacts electrostatically with the proteins present in the cells. However, the nonspecific binding can be reduced with improvised chemical modification of the nanocomplexes in future studies. Third, because of the unique plasmonic properties of the nanocomplexes and tunability in the near IR, they can absorb resonant light and effectively convert light to heat, followed by photothermal therapeutic actuation, resulting in tumor ablation

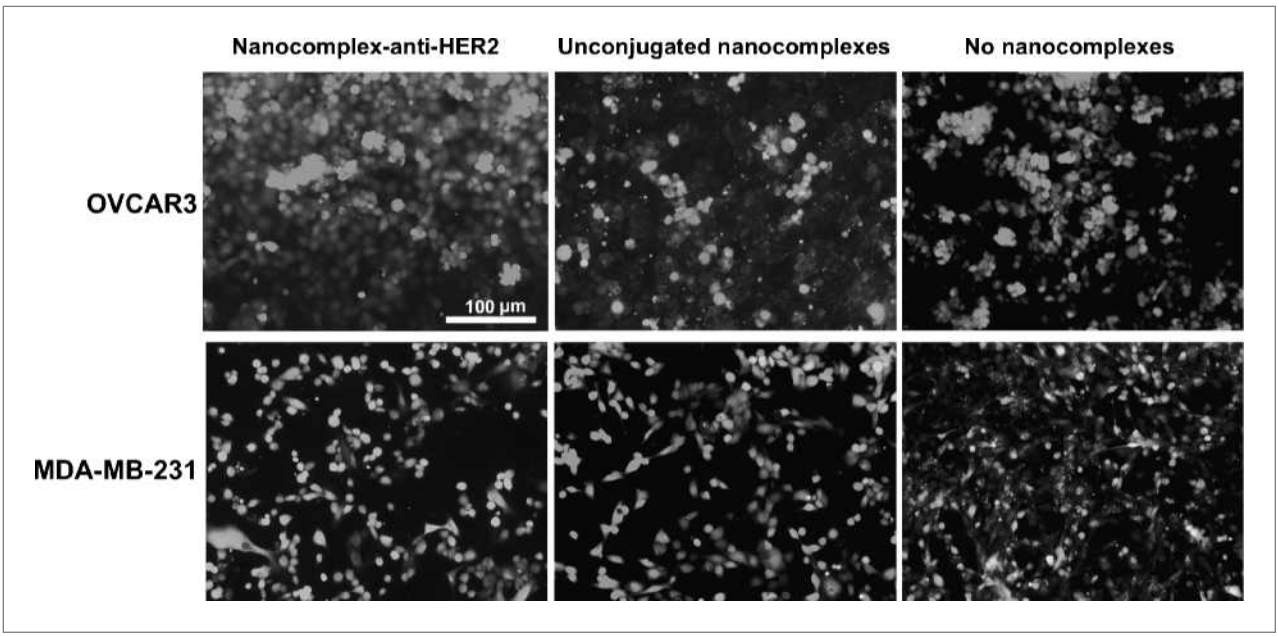

Figure 5. Absence of cytotoxicity on OVCAR3 cells incubated with nanocomplex–anti-HER2 conjugates, unconjugated nanocomplexes, and control (no nanocomplexes) are in the top row. MDA-MB-231 cells incubated with nanocomplex–anti-HER2 conjugates, unconjugated nanocomplexes, and controls are in the bottom row. Live cells are stained green with calcein, and dead cells are stained red with propidium iodide. Original magnification, ×200. Scale bar, 100 μm for all panels.

Published OnlineFirst April 6, 2010; DOI: 10.1158/1535-7163.MCT-09-0829

with near 100% remission rates (13). Fourth, the nanocomplexes have low cytotoxicity and a particle size conducive to passive extravasation from the tumor vasculature (45, 46). This will allow future studies in animal models because these nanocomplexes will accumulate in the tumor enabling simultaneous comprehensive imaging and therapy. In this study, the nanocomplexes have proven beneficial for the treatment of ovarian cancer *in vitro*. Therefore, they can be promising candidates for *in vivo* studies for ovarian cancer models, as well as other tumor types.

In conclusion, this is the first successful integration of dual modal bioimaging with photothermal cancer therapy for the treatment of ovarian cancer cells using a molecularly targeted gold nanoshell-based theranostic probe. Unlike conventional cancer therapy approaches such as radiation therapy or chemotherapy, which can have fatal side effects, nanoshell-based photothermal ablation therapy is benign and safe. Moreover, because of their selective accumulation at cancer cells expressing the HER2 cell receptor, only cells retaining the nanoshells will heat up and ablate when illuminated with near-IR laser, whereas neighboring healthy cells will not experience plasmonic heating. These nanocomplexes can potentially be used as a tool for evaluating transmembrane receptor number, cell viability, and real-time monitoring of cell status. Because cancer predominantly spreads through the blood and lymphatic system, the potential ability to molecularly image cancer cells in metastatic carcinoma without incision and with microdose amounts of safe, nontoxic, multifunctional nanoparticles will have a significant impact on the standard of diagnosis and therapy for many cancers. The low cytotoxicity of these nanocomplexes and their therapeutic efficacy could be potentially beneficial in the study of deep organ metastatic carcinoma in animal models.

Disclosure of Potential Conflicts of Interest

No potential conflicts of interest were disclosed.

Acknowledgments

We thank Prof. Jeffrey G. Jacot (Assistant Professor, Department of Bioengineering, Rice University and Division of Congenital Heart Surgery, Texas Children's Hospital) and Jackson Myers (graduate student, Rice University) for the use of the fluorescence microscope, and Xiande Liu (postdoctoral associate in the Department of Medicine, Baylor College of Medicine) for providing valuable help and discussions.

Grant Support

Baylor College of Medicine faculty startup and seed grant funding (A. Joshi) and seed award 268305012 (W. Chen, M. Bartels, A. Joshi), Robert A. Welch Foundation (C-1220; R. Bardhan and N.J. Halas), Multidisciplinary University Research Initiative (W911NF-04-01-0203; R. Bardhan and N.J. Halas), Air Force Office of Scientific Research (F49620-03-C-0068; R. Bardhan and N.J. Halas), and NIH grant P30DK079638 (C. Perez-Torres and R. Pautler).

The costs of publication of this article were defrayed in part by the payment of page charges. This article must therefore be hereby marked *advertisement* in accordance with 18 U.S.C. Section 1734 solely to indicate this fact.

Received 09/08/2009; revised 12/22/2009; accepted 01/25/2010; published OnlineFirst 04/06/2010.

References

1. Jemal A, Siegel R, Ward E, et al. Cancer statistics. CA Cancer J Clin 2008;58:71–96.
2. Markman M, Rothman R, Hakes T, et al. Second-line platinum therapy in patients with ovarian cancer previously treated with cisplatin. J Clin Oncol 1991;9:389–93.
3. Clark TG, Stewart ME, Altman DG, Gabra H, Smyth JF. A prognostic model for ovarian cancer. Br J Cancer 2001;85:944–52.
4. Camilleri-Broët S, Hardy-Bessard AC, Le Tourneau A, et al. HER-2 overexpression is an independent marker of poor prognosis of advanced primary ovarian carcinoma: a multicenter study of the GINECO group. Ann Oncol 2004;15:104–12.
5. Dimova I, Zaharieva B, Raitcheva S, Dimitrov R, Doganov N, Toncheva D. Tissue microarray analysis of EGFR and erbB2 copy number changes in ovarian tumors. Int J Gynecol Cancer 2006;16:145–51.
6. Felip E, Del Campo JM, Rubio D, Vidal MT, Colomer R, Bermejo B. Overexpression of c-erbB-2 in epithelial ovarian cancer. Prognostic value and relationship with response to chemotherapy. Cancer 1995;75:2147–52.
7. Høgdall EV, Christensen L, Kjaer SK, et al. Distribution of HER-2 overexpression in ovarian carcinoma tissue and its prognostic value in patients with ovarian carcinoma. Cancer 2003;98:66–73.
8. Ross JS, Yang F, Kallakury BV, Sheehan CE, Ambros RA, Muraca PJ. *HER-2/neu* oncogene amplification by fluorescence *in situ* hybridization in epithelial tumors of the ovary. Am J Clin Pathol 1999;111:311–6.
9. Hamilton TC, Young RC, McKoy WM, et al. Characterization of a human ovarian carcinoma cell line (NIH: OVCAR-3)[1] with androgen and estrogen receptors. Cancer Res 1983;43:5379–89.
10. Hellström I, Goodman G, Pullman J, Yang Y, Hellström KE. Overexpression of HER-2 in ovarian carcinomas. Cancer Res 2001;61:2420–3.
11. McCarthy JR. The future of theranostic nanoagents. Nanomed 2009;4:693–5.
12. Davis ME, Chen ZG, Shin DM. Nanoparticle therapeutics: an emerging treatment modality for cancer. Nat Rev Drug Discov 2008;7:771–82.
13. Hirsch LR, Stafford RJ, Bankson JA, et al. Nanoshell-mediated near-infrared thermal therapy of tumors under magnetic resonance guidance. Proc Natl Acad Sci U S A 2003;100:13549–54.
14. O'Neal DP, Hirsch LR, Halas NJ, Payne JD, West JL. Photo-thermal tumor ablation in mice using near infrared-absorbing nanoparticles. Cancer Lett 2004;209:171–6.
15. Huang X, El-Sayed IH, Qian W, El-Sayed MA. Cancer cell imaging and photothermal therapy in the near-infrared region by using gold nanorods. J Am Chem Soc 2006;128:2115–20.
16. Skrabalak SE, Au L, Lu X, Li X, Xia Y. Gold nanocages for cancer detection and treatment. Nanomed 2007;2:657–68.
17. Lu W, Xiong C, Zhang G, et al. Targeted photothermal ablation of murine melanomas with melanocyte-stimulating hormone analog-conjugated hollow gold nanospheres. Clin Cancer Res 2009;15:876–86.
18. Loo C, Lin A, Hirsch L, et al. Nanoshell-enabled photonics-based imaging and therapy of cancer. Technol Cancer Res Treat 2004;3:33–40.
19. Gobin AM, Lee MH, Halas NJ, James WD, Drezek RA, West JL. Near-infrared resonant nanoshells for combined optical imaging and photothermal cancer therapy. Nano Lett 2007;7:1929–34.
20. Loo C, Lowery A, Halas N, West J, Drezek R. Immunotargeted

Published OnlineFirst April 6, 2010; DOI: 10.1158/1535-7163.MCT-09-0829

nanoshells for integrated cancer imaging and therapy. Nano Lett 2005;5:709–11.
21. Hilger I, Hergt R, Kaiser WA. Use of magnetic nanoparticle heating in the treatment of breast cancer. IEE Proc Nanobiotechnol 2005;152:33–9.
22. McCarthy JR, Jaffer FA, Weissleder R. A macrophage-targeted theranostic nanoparticle for biomedical applications. Small 2006;2: 983–7.
23. Pan D, Caruthers SD, Hu G, et al. Ligand-directed nanobialys as theranostic agent for drug delivery and manganese-based magnetic resonance imaging of vascular targets. J Am Chem Soc 2008;130:9186–7.
24. Reddy GR, Bhojani MS, McConville P, et al. Vascular targeted nanoparticles for imaging and treatment of brain tumors. Clin Cancer Res 2006;12:6677–86.
25. Nasongkla N, Bey E, Ren J, et al. Multifunctional polymeric micelles as cancer-targeted, MRI-ultrasensitive drug delivery systems. Nano Lett 2006;6:2427–30.
26. Bagalkot V, Zhang L, Levy-Nissenbaum E, et al. Quantum dot-aptamer conjugates for synchronous cancer imaging, therapy, and sensing of drug delivery based on bi-fluorescence resonance energy transfer. Nano Lett 2007;7:3065–70.
27. Bardhan R, Chen W, Perez-Torres C, et al. Nanoshells with targeted simultaneous enhancement of magnetic and optical imaging and photothermal therapeutic response. Adv Funct Mater 2009;19:3901–9.
28. Oldenburg SJ, Averitt RD, Westcott SL, Halas N. Nanoengineering of optical resonances. Chem Phys Lett 1998;288:243–7.
29. Choi MR, Stanton-Maxey KJ, Stanley JK, et al. A cellular Trojan horse for delivery of therapeutic nanoparticles into tumors. Nano Lett 2007;7:3759–65.
30. Bardhan R, Grady NK, Halas NJ. Nanoscale control of near infrared fluorescence enhancement using Au nanoshells. Small 2008;4: 1716–22.
31. Maeda H, Wu J, Sawa T, Matsumura Y, Hori K. Tumor vascular permeability and the EPR effect in macromolecular therapeutics: a review. J Control Release 2000;65:271–84.
32. Melancon MP, Lu W, Yang Z, et al. *In vitro* and *in vivo* targeting of hollow gold nanoshells directed at epidermal growth factor receptor for photothermal ablation therapy. Mol Cancer Ther 2008;7:1730–9.
33. Stober W, Fink A, Bohn EJ. Controlled growth of mono-disperse silica spheres in the micron size range. J Colloid Interface Sci 1968;26:62–9.
34. Duff DG, Baiker A, Edwards PP. A new hydrosol of gold clusters. 1. Formation and particle size variation. Langmuir 1993;9:2301–9.
35. Kang YS, Risbud S, Rabolt JF, Stroeve P. Synthesis and characterization of nanometer-size Fe_3O_4 and γ-Fe_2O_3 particles. Chem Mater 1996;8:2209–11.
36. Sampath L, Kwon S, Ke S, et al. Dual-labeled trastuzumab-based imaging agent for the detection of human epidermal growth factor receptor 2 overexpression in breast cancer. J Nucl Med 2007;48: 1501–10.
37. Huang YF, Lin YW, Lin ZH, Chang HT. Aptamer-modified gold nanoparticles for targeting breast cancer cells through light scattering. J Nanopart Res 2009;11:775–83.
38. Finn RS, Dering J, Ginther C, et al. Dasatinib, an orally active small molecule inhibitor of both the src and abl kinases, selectively inhibits growth of basal-type/"triple-negative" breast cancer cell lines growing *in vitro*. Breast Cancer Res Treat 2007;105:319–26.
39. Perou CM, Sørlie T, Eisen MB, et al. Molecular portraits of human breast tumours. Nature 2000;17:747–52.
40. Sørlie T, Perou CM, Tibshirani R, et al. Gene expression patterns of breast carcinomas distinguish tumor subclasses with clinical implications. Proc Natl Acad Sci U S A 2001;98:10869–74.
41. Sotiriou C, Neo SY, McShane LM, et al. Breast cancer classification and prognosis based on gene expression profiles from a population-based study. Proc Natl Acad Sci U S A 2003;100:10393–8.
42. Tseng PH, Wang YC, Weng SC, et al. Overcoming trastuzumab resistance in HER2-overexpressing breast cancer cells by using a novel celecoxib-derived phosphoinositide-dependent kinase-1 inhibitor. Mol Pharmacol 2006;70:1534–41.
43. Ray-Coquard I, Guastalla JP, Allouache D, et al. HER2 overexpression/amplification and trastuzumab treatment in advanced ovarian cancer: a GINECO phase II study. Clin Ovarian Cancer 2008;1:54–9.
44. Reese DM, Slamon DJ. HER-2/neu signal transduction in human breast and ovarian cancer. Stem Cells 1997;15:1–8.
45. Kong G, Braun RD, Dewhirst MW. Hyperthermia enables tumor-specific nanoparticle delivery: effect of particle size. Cancer Res 2000;60:4440–5.
46. Kong G, Braun RD, Dewhirst MW. Characterization of the effect of hyperthermia on nanoparticle extravasation from tumor vasculature. Cancer Res 2001;61:3027–32.

Published OnlineFirst April 6, 2010; DOI: 10.1158/1535-7163.MCT-09-0829

Molecular Cancer Therapeutics

A Molecularly Targeted Theranostic Probe for Ovarian Cancer

Wenxue Chen, Rizia Bardhan, Marc Bartels, et al.

Mol Cancer Ther 2010;9:1028-1038. Published OnlineFirst April 6, 2010.